HAL
open science

Mechanical behavior of terra cotta ceramics characterized by kinematic full-field measurements

Vincent Huon, Bertrand Wattrisse, Moulay Saïd El Youssoufi, Andre Chrysochoos

To cite this version:

Vincent Huon, Bertrand Wattrisse, Moulay Saïd El Youssoufi, Andre Chrysochoos. Mechanical behavior of terra cotta ceramics characterized by kinematic full-field measurements. Journal of Materials in Civil Engineering, 2007, 19, pp.642-647. 10.1061/(ASCE)0899-1561(2007)19:8(642) . hal-00572430

HAL Id: hal-00572430

https://hal.science/hal-00572430v1

Submitted on 1 Jun 2023

HAL is a multi-disciplinary open access archive for the deposit and dissemination of scientific research documents, whether they are published or not. The documents may come from teaching and research institutions in France or abroad, or from public or private research centers.

L'archive ouverte pluridisciplinaire **HAL**, est destinée au dépôt et à la diffusion de documents scientifiques de niveau recherche, publiés ou non, émanant des établissements d'enseignement et de recherche français ou étrangers, des laboratoires publics ou privés.

Mechanical Behavior of Terra Cotta Ceramics Characterized by Kinematic Full-Field Measurements

Vincent Huon[1]; Bertrand Wattrisse[2]; Moulay Saïd El Youssoufi[3]; and André Chrysochoos[4]

Abstract: The lamellate structure of clay and the extrusion forming process cause terra cotta ceramic's anisotropic elastic behavior at low strain and may induce gradients of macroscopic mechanical properties. Among other techniques, strain measurements obtained through digital image correlations were used to locally characterize transverse isotropic elastic behavior. Kinematic field measurements on small specimens were also compared with fields derived from three-dimensional finite element computations in order to check the consistency of the local characterization procedure.

Keywords: Mechanical properties; Clays; Measurement; Construction materials.

Introduction

Terra cotta ceramics are often used in residential house building. They are nearly always associated with other civil engineering materials, e.g., terra cotta beams with a core of prestressed concrete are widely used for building floors, terraces, or flat roofs. In this kind of composite element, terra cotta serves as a sacrificial formwork, i.e., concrete is considered to be the only material that supports prestressing forces. However, from a mechanical standpoint, terra cotta has remarkable strengths (i.e., often better than those of standard concrete) that are often not effectively utilized. The work presented in this paper is a part of an overall study carried out to characterize the anisotropic thermohygromechanical behavior of terra cottas used as building material in civil engineering projects. From an industrial standpoint, the goal is to develop numerical computer-aided design tools that can be used to optimize structural elements. This optimization must simultaneously take into account parameters related to thermal comfort and those associated with the mechanical strength of the designed structure.

In the recent past, the classical use of terra cotta bricks did not require in-depth knowledge on their mechanical properties, since they were mainly loaded in compression. Now, the use of the terra cotta as a composite structural component calls for a more rigorous analysis of its contribution to the overall behavior of the structure. Thus, we studied the heterogeneous and anisotropic properties of this material using strain field measurements. These measurements were obtained by digital image correlation (DIC) techniques with the aim of checking the degree of heterogeneity of the ceramic structures and characterizing the anisotropy of the terra cotta.

This paper is structured as follows: First, we review the material properties that led us to propose a transverse isotropic model to describe the elasticity of ceramics. Second, we show how the elastic parameters were locally derived from tests conducted on elementary structures considered as representative volumes of the material. Finally, to check the influence of the discrepancy noted in the elastic constants, we compare strain patterns predicted by a three-dimensional (3D) finite element (FE) computation with those obtained by the DIC.

Terra Cotta

Argillaceous soils are the primary products for manufacturing terra cotta. In most cases, they are used with additives (sand, limestone, etc.) to enhance the characteristics of structural elements, or to modify the functional characteristics or the aspect of the finished products. Clays are hydrated aluminosilicates whose lamellar structure can fix a certain quantity of water between folia. Four stages are required to obtain the end product:

1. Preparation: To obtain an argillaceous mixture after proportioning and crushing the components;
2. Forming: Generally by extrusion;
3. Drying: To eliminate almost all of the water used during the forming stage; and
4. Firing: The duration depends on the size of the terra cotta components, generally within the 800–1,200 °C temperature range.

These different stages induce an anisotropic and heterogeneous thermomechanical behavior of the terra cotta structural elements. The extrusion process involves a privileged direction and

[1]Laboratoire de Mécanique et Génie Civil, UMR 5508 CNRS—UMII, cc 048, Université Montpellier II, Place Eugène Bataillon, 34095 Montpellier Cedex 05, France. E-mail: huon@lmgc.univ-montp2.fr

[2]Laboratoire de Mécanique et Génie Civil, UMR 5508 CNRS—UMII, cc 048, Université Montpellier II, Place Eugène Bataillon, 34095 Montpellier Cedex 05, France. E-mail: wattriss@lmgc.univ-montp2.fr

[3]Laboratoire de Mécanique et Génie Civil, UMR 5508 CNRS—UMII, cc 048, Université Montpellier II, Place Eugène Bataillon, 34095 Montpellier Cedex 05, France. E-mail: elyouss@lmgc.univ-montp2.fr

[4]Laboratoire de Mécanique et Génie Civil, UMR 5508 CNRS—UMII, cc 048, Université Montpellier II, Place Eugène Bataillon, 34095 Montpellier Cedex 05, France. E-mail: chryso@lmgc.univ-montp2.fr

leads to transverse isotropy of the material. This also induces gradients of elastic properties throughout the structure, especially between the boundary and the core of the extruded parts. These gradients are often amplified and disturbed by the drying and firing processes, because of mass and heat transfers, by the material heterogeneity due to the irregular distribution of the pores, and the varied size grains of the mixture despite the preparation stage. We used sets of specimens randomly extracted from an extruded structure to estimate discrepancies in the elastic parameters.

To define transverse isotropy axes, we introduced L as the direction of extrusion, T as the direction across the layers of terra cotta, and R as the direction in the plane of the layers, i.e., orthogonal with L and T (Fig. 1). The five elastic constants to be determined are then: Young's moduli $E_L=E_R$ and E_T; Poisson's ratios ν_{LR} and $\nu_{LT}=\nu_{RT}$; Shear moduli $G_{LT}=G_{RT}$. Due to the isotropy of the plane of the layers, the shear modulus G_{LR} can be written as $G_{LR}=E_L/[2(1+\nu_{LR})]$. Using engineering notations, the strain-stress relationship may be written as

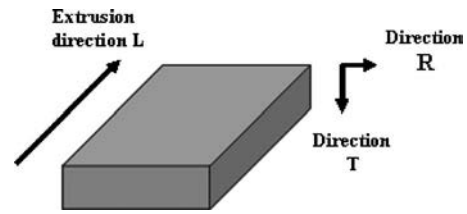

Fig. 1. Directions of transverse isotropy

$$\begin{pmatrix} \varepsilon_{LL} \\ \varepsilon_{RR} \\ \varepsilon_{TT} \\ \varepsilon_{LR} \\ \varepsilon_{RT} \\ \varepsilon_{LT} \end{pmatrix} = \begin{bmatrix} \frac{1}{E_L} & -\frac{\nu_{LR}}{E_L} & -\frac{\nu_{LT}}{E_L} & 0 & 0 & 0 \\ -\frac{\nu_{LR}}{E_L} & \frac{1}{E_L} & -\frac{\nu_{LT}}{E_L} & 0 & 0 & 0 \\ -\frac{\nu_{LT}}{E_L} & -\frac{\nu_{LT}}{E_L} & \frac{1}{E_T} & 0 & 0 & 0 \\ 0 & 0 & 0 & \frac{1+\nu_{LR}}{E_L} & 0 & 0 \\ 0 & 0 & 0 & 0 & \frac{1}{2G_{LT}} & 0 \\ 0 & 0 & 0 & 0 & 0 & \frac{1}{2G_{LT}} \end{bmatrix} \begin{pmatrix} \sigma_{LL} \\ \sigma_{RR} \\ \sigma_{TT} \\ \sigma_{LR} \\ \sigma_{RT} \\ \sigma_{LT} \end{pmatrix} \tag{1}$$

where ε_{IJ} and σ_{IJ}=matrix components of the strain and stress tensors with respect to the *LRT* frame.

Experimental Protocol

Material and Specimens

An electron probe microanalysis (EPM) was used to determine the grain size and nature. The maximum grain size was 1 mm, including:

- Quartz grains (the most common);
- Calcite grains of up to 200 μm in size (the least common); and
- A low percentage of small feldspath grains.

The chemical composition of the terra cotta studied in this paper is given in Table 1.

Building engineering standards do not give any dimensional specifications for terra cotta specimens. Moreover, in the scientific literature, we found no examples of terra cotta specimens adapted for classical mechanical tests such as tension compression tests, shearing, and bending tests. Thus, we based our study on guidelines for the characterization of cements or mortars with granular sizes similar to that of terra cotta. Although compression tests are generally performed on specimens with a ratio of 2, we decided to use cubic samples of reduced sizes (sides: 15 mm) in order to ensure an adequate homogeneity of these elementary structures at the risk of getting a triaxiality effect due to the compression plates. The specimens were machined using a water jet cutting process to avoid geometrical defects. The compression tests, performed on cubic samples with transverse isotropy axes, gave access to the three elastic moduli and the three Poisson ratios.

The shear modulus G_{LR} was determined in the shearing zone of the Y-shaped specimen whose cross section is given in Fig. 2. For this type of geometry, it is easy to obtain a layer plane parallel

Table 1. Chemical Composition of Terra Cotta

Elements	Atomic %
Silicon dioxide (SiO_2)	57.9
Alumina (Al_2O_3)	15.4
Lime (CaO)	14.4
Iron oxide (Fe_2O_3)	4.9
Titania (TiO_2)	0.4
Magnesia (MgO)	1.4
Potash (K_2O)	4.3
Soda (Na_2O)	1.3

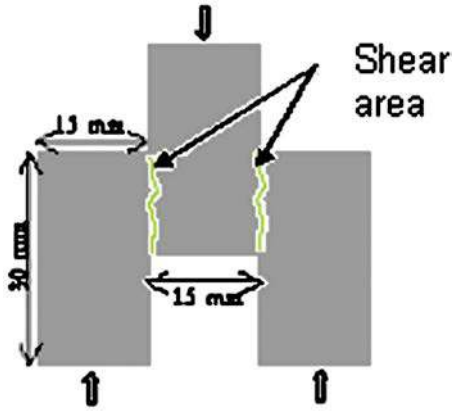

Fig. 2. Y-shaped specimen

to the cross section. Conversely, the extrusion process does not allow shearing of the specimen leading to a measurement of G_{LT} and G_{RT}. Indeed, the specimen size in the direction T (Fig. 1) must be limited to insure a homogeneous firing in the samples. At this level, ultrasonic goniometry measurements were used to determine both the missing shear moduli, to check the modulus estimates, and the Poisson's ratios obtained mechanically (Preziosa et al. 1981; Baudouin and Hosten 1997).

Experimental Setup

The experimental setup involved a 100 kN tension-compression servomechanical testing machine. Digital images were recorded during the test by a charge coupled device (CCD) camera set in front of the sample, Fig. 3. The lens axis of the camera was fixed according to the frame of the testing machine and remained perpendicular to the surface of the sample. The CCD sensor had eight square megapixels distributed in a 3,500 line × 2,300 column grid. The camera provided maximum space resolution from

Fig. 3. Experimental device—testing machine coupled to a digital video camera

0.01–0.02 mm/pixel with the "macro" lens used during the tests. For images of maximum size, the camera can capture up to five images a second digitized in eight bits.

Displacement and Strain Measurements

The inplane displacement components were computed by a direct DIC algorithm on each point $M_0(i_0,j_0)$ of a virtual grid defined in the reference configuration. The position of the discrete maximum of the discrete intercorrelation function φ gives the displacement of point M_0 with a one pixel resolution. Between two images, I_1 and I_2, separated by a small strain increment, φ is written as

$$\underset{(k,l)\in\left[\frac{-RZ}{2},\frac{RZ}{2}\right]}{\varphi(k,l)} = \frac{\sum_{i-i_0=-CZ/2}^{CZ/2}\sum_{j-j_0=-CZ/2}^{CZ/2} I_1(i,j)\cdot I_2(i+k,j+l)}{\sqrt{\sum_{i-i_0=-CZ/2}^{CZ/2}\sum_{j-j_0=-CZ/2}^{CZ/2} I_1^2(i,j)}\cdot\sqrt{\sum_{i-i_0=-CZ/2}^{CZ/2}\sum_{j-j_0=-CZ/2}^{CZ/2} I_2^2(i+k,j+l)}} \tag{2}$$

In Eq. (2), CZ stands for the correlation zone [i.e., the M_0 neighborhood defining the optical signature of "point" $M_0(i_0,j_0)$], and RZ=research zone (i.e., the M_0 neighborhood where the optical signature is tracked). These zones correspond to the domain of variation of (i,j) and (k,l), respectively. To obtain subpixel measurements, we used a polynomial interpolation of φ in the vicinity of its discrete maximum (Oulamara et al. 1988).

Heterogeneous strain field analysis considers small "gauge lengths" that induce a poor signal-to-noise ratio. Consequently, a local least-squares fitting of the displacement data is performed before any differentiation: The displacement field is locally approximated in the neighborhood of each point M_0 by a given function. Both the shape of the approximation function and the size of the approximation zone (AZ) may affect the accuracy of the strain measurement. Here, bilinear functions were used as they are associated with a locally constant deformation. For more information, the reader may refer to (Wattrisse et al. 2001). The image processing performance was tested, respectively, in experimental and analytic cases corresponding to rigid body motion and to homogeneous or heterogeneous strain (Wattrisse et al. 2002). Indeed, analytical checks were necessary, because it is impossible to impose a given strain field to a real material specimen.

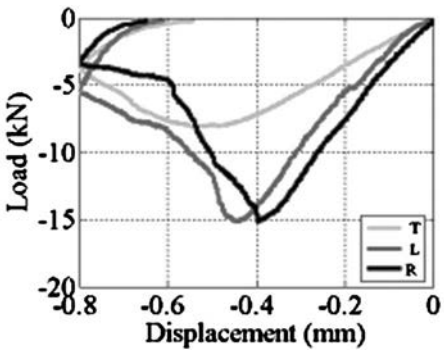

Fig. 4. Compression tests according to the directions *R*, *L*, and *T*—Sample responses

Experimental Results

Global Response of the Samples

The compression tests, performed at constant velocity ($0.1\ \mathrm{mm\,s^{-1}}$), were initially conducted on cubic specimens in the three directions *L*, *R*, and *T*. Fig. 4 illustrates the results obtained. This feature is consistent with the transverse isotropy hypothesis. At the beginning of the loading process, the cubic structure has an elastic response until the maximum load was reached. Then, the softening part of the curve corresponds to the propagation of microcracks throughout the sample. Compression in the direction *T* was performed perpendicular to the plane of the layers. This configuration gave the structure greater compliance and seemed to be less favorable for the propagation and coalescence of microscopic cracks.

Material Response

Based on previous results, the tests were carried out, while limiting maximum compressive loading in order to ensure an elastic response of the structure. These tests were performed at constant velocity ($0.1\ \mathrm{mm\,s^{-1}}$ during loading and $0.5\ \mathrm{kN\,s^{-1}}$ during unloading). The strain field measurements were first used to check the boundary conditions during loading. Some examples of strain patterns obtained by DIC are shown in Fig. 5 and correspond to components $\varepsilon_{\mathrm{LL}}$ and $\varepsilon_{\mathrm{TT}}$ of the strain tensor. Both fields were extracted from a compression test in direction *L* at maximum loading ($\approx$11 kN).

We observed slightly heterogeneous deformation fields, which were not in full agreement with the kinematics of a simple compression test. The strain level curve distributions highlighted that this nonuniformity was partly due to the boundary conditions at

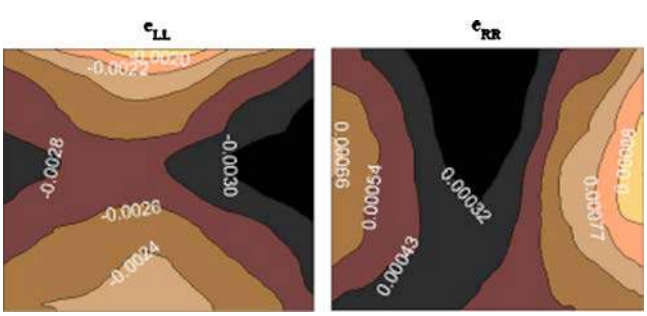

Fig. 5. $\varepsilon_{\mathrm{LL}}$ and $\varepsilon_{\mathrm{RR}}$ strain—Compression in the direction *L*

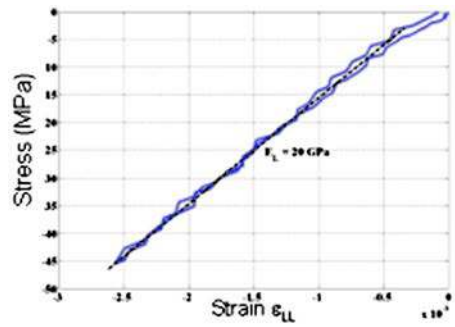

Fig. 6. Stress-strain diagram for a compression test in the *L* direction associated with a load-unload cycle

the specimen surfaces in contact with the compression plates. The irregular patterns noted for level curves could also have been associated with the material heterogeneities and, of course, with the noise on strain measurements. The fields could be interrelated with the FE calculation using displacement boundary conditions corresponding to those observed experimentally. The stress-strain curve corresponding to measurements obtained in the central area of the specimen is plotted in Fig. 6. The compression strain $\varepsilon_{\mathrm{LL}}$ is directly derived from speckle image processing, while the compression stress σ_{LL} is determined by assuming a uniform stress distribution over the cross section. Then, a simple regression is used to estimate the elasticity modulus (E_{L} in Fig. 6). All results for the estimation of Young's modulus are given in Table 2. Note that the standard deviations obtained on moduli using a random set of about ten samples were about 4 GPa for mean values of about 20 GPa. This discrepancy is very substantial and illustrates the heterogeneity between specimens.

Fig. 7 presents estimates of Poisson ratio $\nu_{\mathrm{LT}}=-\varepsilon_{\mathrm{TT}}/\varepsilon_{\mathrm{LL}}$ for different $\varepsilon_{\mathrm{LL}}$. As previously underlined, this computation assumes a uniform compression state in the central part of the sample. The increasing discrepancy of measurements observed when strain components were around zero was associated with degradation of the signal to noise ratio. Therefore, only estimates of the Poisson's ratios for $|\varepsilon_{\mathrm{LL}}|>5\times10^{-4}$ were considered. Tests were performed on Y-shaped specimens to determine the shear modulus G_{LR} (see Fig. 2). These tests were performed at constant velocity ($0.01\ \mathrm{mm\,s^{-1}}$ during loading and $0.5\ \mathrm{kN\,s^{-1}}$ during unloading). We noted two phases in the structural response: The first corresponded to a quasielastic behavior, while the second started with the inception of the first macroscopic crack. Fig. 8 illustrates the potentials of correlation methods regarding microcrack detection. The displacement field features (here, component U_{L}) enabled us to visualize crack onset and propagation at the sample surface as soon as its opening was not parallel to the direction of the chosen displacement component. The amplitude of the displacement discontinuity may be related to the crack opening.

Fig. 10 presents the $\varepsilon_{\mathrm{RL}}$ distribution and shows the significant sliding ("shearing") zones. In these zones, we estimated a mean

Table 2. Average Value and Standard Deviation of Experimental Results Obtained for E_L, E_R, and E_T

	Number of tests	Average value (GPa)	Standard deviation (GPa)
E_L	10	20.2	2.8
E_R	6	19.8	3.1
E_T	8	5	0.3

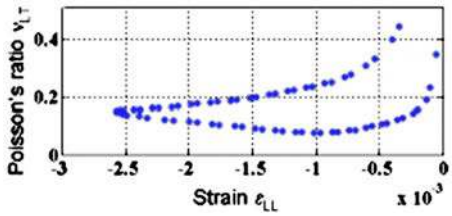

Fig. 7. Evolution of the Poisson's ratio ν_{LT} associated with the loading in Fig. 6

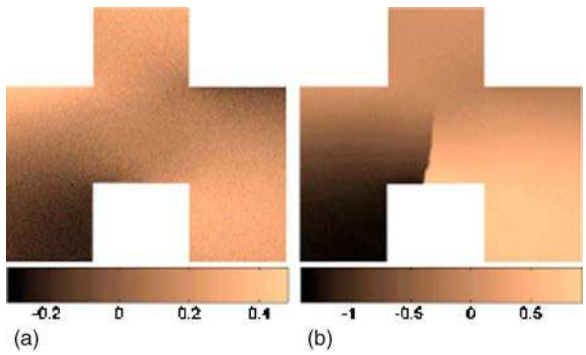

Fig. 8. Displacement pattern of u_L (a) fissuring; (b) propagation

shear stress and a mean sliding strain to obtain the G_{LR}. As mentioned above, the other shear moduli were classically obtained using ultrasonic techniques. The average elasticity constant values we obtained are: $E_L=E_R=20$ GPa; $E_T=5$ GPa; $\nu_{LR}=0.17$, $\nu_{LT}=\nu_{RT}=0.15$; and $G_{LR}=8.8$ GPa, $G_{LT}=G_{RT}=3$ GPa.

Validity Checks

Cubic Specimens

The elastic modulus estimates were checked by comparing the local stress values obtained in the central area by 3D FE computations with the compression stress deduced from the loading data. The numerical model takes transverse isotropy elasticity into account and supposes that the material is homogeneous. The elasticity tensor takes the predetermined mean values into account. It also supposes that the axis of compression is one of the transverse isotropy axes. Loading was modeled by displacement fields imposed at the surfaces in contact with the compression plates. These boundary conditions were directly extracted from the displacement data obtained by DIC. Fig. 9 presents the results obtained for a simulated compressive test in the L direction. Considering a cross section placed in the medium part of the specimen, computations enabled us to estimate, at maximum elastic loading, a mean value for the compression stress pattern $(\bar{\sigma}_{LL})_{comp}$ of about 44.5 MPa. The standard deviation associated with this distribution was about 0.6 MPa. Hence, the stress state, imposed by the experimental boundary conditions, was uniform in a first good approximation. Compression stress $(\sigma_{LL})_{exp}$ can also be estimated assuming, as usual, a uniform stress state over the cross section and using the load measurements. We found that $(\sigma_{LL})_{exp}$ was about 43.5 MPa. The difference between $(\sigma_{LL})_{exp}$ and $(\bar{\sigma}_{LL})_{comp}$ remained small, thus, partly confirming the previous approximations.

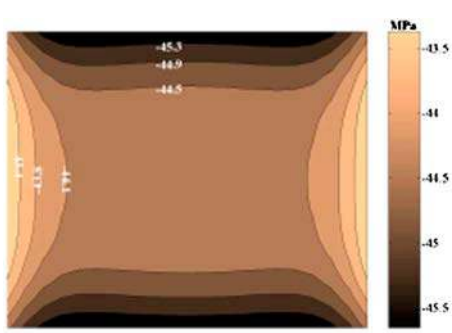

Fig. 9. Normal stress field on the middle cross section

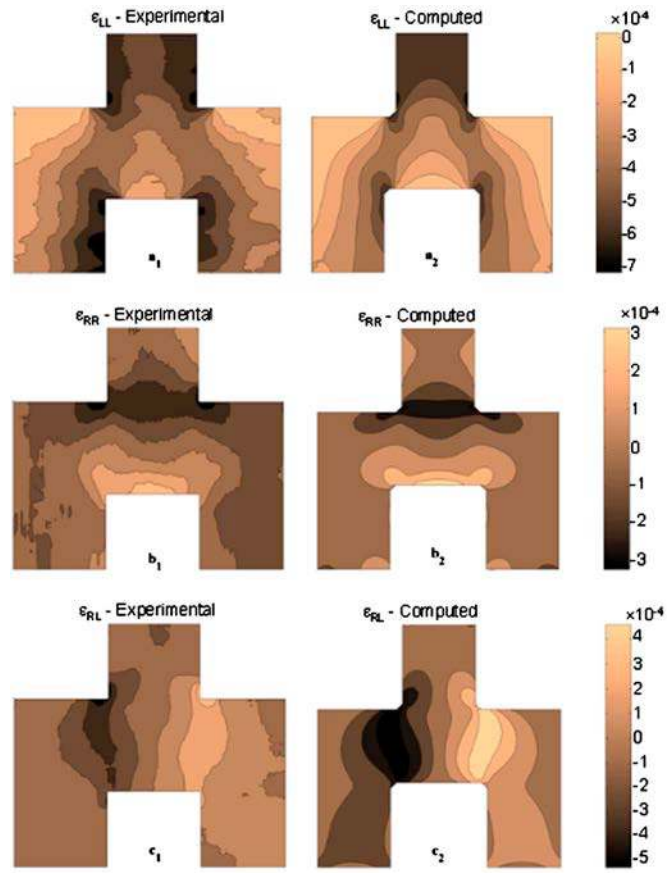

Fig. 10. Fields of strain: (1) derived from digital image correlation; (2) 3D FE calculation

Y-Shaped Specimens

We checked the overall consistency of the characterization procedure by comparing strain fields obtained in Y-shaped samples with those resulting from FE computations. Loading was modeled by displacements obtained by DIC imposed at surfaces in contact with the compression plates. The computed and experimental strain patterns are compared in Fig. 10. We noted a satisfactory global correlation between both distributions, regardless of the strain tensor component. Moreover, we noted a close correlation between the measurement and the calculation when comparing the overall loading applied to the structure (Table 3).

Table 3. Compression Load Supported by the Y-shaped Sample: Measurement and Computation

	F_{exp} (kN)	E_{comp} (kN)
$t=6$ s	0.32	0.37
$t=12$ s	2.17	2.36

Conclusion

The results presented in this paper highlight the benefits of digital correlation techniques for characterizing and identifying the mechanical behavior of a traditional civil engineering material. Full field measurements were initially useful for checking the quality of the tests by analyzing the characteristics of the displacement fields near surfaces where loading boundary conditions were imposed. The kinematic data were also useful for the evaluation of elasticity constants of a transverse isotropic behavior model. A comparison between experimental and numerical results obtained on a Y-shaped terra cotta brick element showed that the set of identified elastic constants gave satisfactory results. To estimate the different elastic parameters and to perform 3D FE computations, we assumed that the material was and remained homogeneous during mechanical transformation. Other very promising approaches will be available in the near future (Geymonat et al. 2002; Claire et al. 2003; Bonnet and Constantinescu 2005) to consider the local elastic properties of the material and to account for the structural heterogeneities leading to property gradients in civil engineering structures. The capabilities of these inverse approaches are presently being tested on academic (numerical) examples (Latourte et al. 2005). In the near future, they will be applied to noisy and discrete data fields obtained by DIC.

Acknowledgments

The writers would like to thank Saverdun Terre Cuite (STC), a French terra cotta building component manufacturer, for partly supporting this research work.

References

Baudouin, S., and Hosten, B. (1997). "Comparison between prediction and measurement of viscoelastic moduli composite materials versus temperature using ultrasonic immersion technique with oil." *J. Acoust. Soc. Am.*, 102(6), 3,450–3,457.

Bonnet, M., and Constantinescu, A. (2005). "Inverse problems in elasticity." *Inverse Probl.*, 21, 1–50.

Claire, D., Roux, S., and Hild, F. (2003). "Identification de conductivités thermiques et de propriétés élastiques locales par analyse de champs." *Mécanique and Industries*, 4(6), 655–665.

Geymonat, G., Hild, F., and Pagano, S. (2002). "Identification of elastic parameters by displacement field measurement." *C. R. Mec.*, 330, 403–408.

Latourte, F., Chrysochoos, A., Geymonat, G., Pagano, S., and Wattrisse, B. (2005). "Identification of elastoplastic constitution equations parameters using digital image correlation." *Proc., ICEM-SEM 2005, Optical Method and Inverse Identification*, (CD-ROM), Portland.

Oulamara, A., Tribillon, G., and Duvernoy, J. (1988). "Subpixel speckle displacement measurement using a digital processing technique." *J. Mod. Opt.*, 37, 1,201–1,211.

Preziosa, C., Mudry, M., Launay, J., and Gilletta, F. (1981). "Détermination des constantes élastiques du bois par une méthode acoustique goniométrique." *C. R. Acad. Sc. Paris, Série II*, t. 293, 91–94.

Wattrisse, B., Chrysochoos, A., Muracciole, J.-M., and Némoz-Gaillard, M. (2001). "Analysis of strain localization during tensile tests by digital image correlation." *Exp. Mech.*, 41(1), 29–39.

Wattrisse, B., Muracciole, J.-M., and Chrysochoos, A. (2002). "Strain measurements by local least-squares fitting of displacement field obtained by digital image correlation—Calibration of the method." *Proc., ASTM Symp. Full-Field Optical Deformation Measurements: Applications and User Experience*, ASTM, West Conshohoken, Pa.